Chemical Vapor Transformation of Lithium Metal: Mechanism and Enhanced Stability

Kyobin Park[1], Yu Lim Kim[2], Justin G. Connell[3], Cong Liu[2], Hacksung Kim[2,4], Sungjoon Kim[1], Chi Thang Nguyen[1], Anil U. Mane[1], Donghyeon Kang[1], and Jeffrey W. Elam[1**]*

[1]Applied Materials Division, Argonne National Laboratory, Lemont, IL 60439, USA

[2]Chemical Sciences and Engineering Division, Argonne National Laboratory, Lemont, IL 60439, USA

[3]Materials Science Division, Argonne National Laboratory, Lemont, IL 60439, USA

[4]Center for Catalysis and Surface Science, Northwestern University, Evanston, IL 60208, USA

[*]Correspondence: dhkang@anl.gov

[**]Correspondence: jelam@anl.gov

Keywords: atomic layer deposition, chemical vapor transformation, SEI, amorphous carbon, Li metal, Li-Al alloy

ABSTRACT

Constructing a stable solid electrolyte interface (SEI) with high productivity and scalability is essential for practical application of thin Li metal anodes. Here, we report a chemical vapor transformation (CVT) strategy in which Li metal is exposed to trimethylaluminum (TMA), inducing a rapid and spontaneous surface reaction that forms a robust, multi-layered SEI. *In situ* quartz crystal microbalance (QCM) and quadrupole mass spectrometry (QMS), combined with *ex situ* X-ray photoelectron spectroscopy (XPS), UV Raman spectroscopy, and density functional theory (DFT) calculations, reveal that TMA removes the native passivation layer, reacts with Li metal, and drives a coupled bulk-surface transformation involving Li-Al interdiffusion. The resulting SEI exhibits a chemically graded structure consisting of an inner Li-Al alloy and an outer amorphous carbon layer, formed via demethylation and ligand-exchange pathways. This modified surface exhibits significantly enhanced stability compared to bare Li in electrochemical cycling using liquid and solid-state electrolytes. This work unveils a unique surface-mediated bulk transformation mechanism for lithium metal and establishes CVT as a scalable and fundamentally distinct approach for interfacial engineering of reactive metals.

1. INTRODUCTION

The development of high energy density batteries is not only a technological necessity but also a cornerstone for driving innovation in cutting-edge applications.[1,2] In this regard, Li metal anodes are considered a promising material for achieving high energy density batteries, including all-solid-state batteries (ASSBs), Li-metal batteries (LMBs), and Li-sulfur batteries, due to their high theoretical capacity (3860 mA h g^{-1}) and low reduction potential (–3.04 V vs. standard hydrogen electrode).[3,4] However, the practical application of Li metal anodes faces considerable challenges, primarily due to the instability of the solid electrolyte interface (SEI), which arises from parasitic reactions between Li metal and electrolytes, ultimately leading to dendrite growth, dead lithium formation, and substantial increases in both volume and impedance.[5] Moreover, to enable Li metal batteries to surpass the energy density of commercial Li-ion batteries with graphite anodes, the Li metal anode thickness should be approximately 50 μm or less.[6,7] Such thin foils are typically produced by rolling extruded Li ingots, a process that commonly utilizes lubricants to control tension and ensure uniform thickness.[8,9] However, during this process, native passivation components such as Li_2CO_3, Li_2O, and LiOH, inevitably form on the Li metal surface even under an inert atmosphere.[10] These heterogeneously distributed layers exhibit variations in conductivity, thickness, and mechanical stability, resulting in uneven Li-ion transport, localized overpotentials, and areas of high current density.[11,12] For this reason, establishing a stable and uniform SEI layer while minimizing the accumulation of byproducts at the interface is critical for maintaining the electrochemical performance of Li metal anodes.

Over the past few decades, atomic layer deposition (ALD) has been extensively studied for its significant advantages in surface and interface engineering for energy storage materials, owing to its ability to create conformal coatings with precisely controlled atomic-scale thickness and

composition. Various coating materials including metal oxides (*e.g.*, Al_2O_3, from trimethylaluminum and H_2O, ZrO_2 (from tetrakis(dimethylamido)zirconium and H_2O),[13-16] fluorides (*e.g.*, LiF from lithium tert-butoxide and HF-pyridine),[17,18] phosphates (*e.g.*, Li_3PO_4 from lithium tert-butoxide and trimethyl phosphate),[19] and sulfides (*e.g.*, Li_xAl_yS from lithium tert-butoxide, tetrakis(dimethylamido)aluminum, and H_2S), [20] have been applied to Li metal to fulfill multiple functions: preventing direct contact with electrolytes, serving as physical barriers against dendrite growth, and facilitating a uniform Li^+ flux.

While these studies have primarily focused on the electrochemical behavior of coated Li metal, they often overlook the underlying ALD growth mechanism on the highly reactive Li surface. In many cases, the thicknesses of ALD layers on the Li metal are estimated based on the number of ALD cycles, under the assumption that ALD proceeds on Li metal similarly to conventional surfaces such as hydroxylated silicon. However, unlike conventional ALD where gas-phase precursors react in a self-limiting manner with surface functional groups (*e.g.*, hydroxyl groups), dopants, or defect sites on the target material, ALD on Li metal may exhibit non-self-limiting behavior, particularly during the initial growth cycles. Indeed, enhanced Al_2O_3 growth on Li metal during the early stages of ALD was observed in the previous work, with growth rates reaching up to 5.5 Å/cycle over the first 1–10 ALD cycles,[14] compared to ~ 1.2 Å/cycle on hydroxylated silicon.[21] This observation suggested a unique growth mechanism which might be influenced by direct reactions between the ALD precursors and the Li surface or its native passivation layers.[22] Building upon these observations, we identified a distinct chemical interaction between freshly exposed Li metal and the trimethylaluminum (TMA) precursor. This reaction, which produces a black coating layer on Li metal almost instantaneously upon TMA exposure, deviates from conventional ALD behavior and prompted further investigation. We define this process as

chemical vapor transformation (CVT) – a rapid and reproducible surface modification process with promising implications for Li metal protection.

In this study, we elucidate the underlying mechanism of CVT, focusing on the chemical interaction between TMA, a common precursor for Al_2O_3 ALD, and 20 μm Li metal to regulate interfacial layer formation on electrodes for sulfide-based ASSBs and LMBs with carbonate-based liquid electrolytes. Unlike conventional Al_2O_3 ALD, which involves alternating exposure to TMA and H_2O, the CVT process utilizes a single TMA exposure with extended dosage time to facilitate the reaction with Li metal and surface impurities. The CVT mechanism between TMA and Li metal was investigated using *in situ* quartz crystal microbalance (QCM), *in situ* quadrupole mass spectrometry (QMS), UV Raman spectroscopy, field emission scanning electron microscopy (FE-SEM), and X-ray photoelectron spectroscopy (XPS) measurements and density functional theory (DFT) calculations. Following the CVT process, spherical morphology measuring several hundred nanometers in diameter consisting of a lithium-aluminum (Li–Al) alloy and an amorphous carbon layer formed on the Li surface. Moreover, we found that the native SEI layer on the Li metal surface including carbonates and oxides was effectively removed during the process. In our work, SEI refers to the native interfacial layer on Li metal as well as the modified surface layer generated by CVT. As a result, 20 μm Li anodes subjected to TMA CVT for 5 seconds (TMA-5s) yielded significantly enhanced cycling stability compared to bare Li. Specifically, TMA-5s|Li_6PS_5Cl (LPSCl)|TMA-5s symmetric cells achieved a cycle life up to seven times longer, and TMA-5s|1.2 M $LiPF_6$ in EC/EMC (3/7, w/w)|TMA-5s symmetric cells lasted more than twice as long. More importantly, the entire CVT process was completed in a short time (a few seconds) and in a single step, highlighting its potential for improving scalability and productivity in fabricating stable interfacial layers for thin Li metal anodes. These findings elucidate the critical role of CVT in

stabilizing Li metal surfaces, paving the way for the development of high-performance energy storage devices including ASSBs with limited Li metal anodes. To the best our knowledge, this is the first report of a “bulklike” chemical transformation of metallic Li upon TMA exposure that may have been overlooked in previous reports of ALD coatings on Li, and possible reasons for this oversight will be discussed below.

2. RESULTS AND DISCUSSION

2.1 Mechanism of SEI formation on Li metal by TMA CVT

To investigate the mechanism of SEI layer formation by TMA CVT on Li metal, we utilized a custom ALD reactor equipped with *in situ* QCM connected to an Ar-filled glovebox (Figure 1a). First, a quartz crystal sensor was coated with Li metal using electron beam evaporation under ultrahigh vacuum, resulting in a thickness of approximately 500 nm. For comparison, a quartz sensor coated with ALD Al_2O_3 was also evaluated. Figures 1b, c shows the mass changes recorded during *in situ* QCM measurements on the Li-coated and Al_2O_3-coated quartz crystal sensors, along with the pressure variations in the reactor, as a function of time during 40 successive TMA exposures. The mass change per unit area (Δm) was calculated by measuring the shift in the resonant frequency (Δf) of the quartz electrode, as described by the Sauerbrey equation:[23]

$$\Delta m = \frac{-(\rho_q \mu_q)^{1/2}}{2{f_0}^2} \Delta f \qquad (1)$$

where ρ_q represents the density of quartz (2.648 g cm^{-3}), μ_q is the shear modulus of quartz (2.947 × 10^{11} g cm^{-1} s^{-2}), and f_0 is the initial frequency of the resonator. It is important to note that factors such as temperature, pressure, viscosity of the surrounding medium, and surface roughness can also influence changes in the resonant frequency.[24] However, since the experiment was conducted under consistent conditions of 150 °C, 1.2 Torr pressure (with approximately 0.1 partial pressure variation), and a flow rate of 40 sccm, we considered that temperature, pressure, and viscosity did not significantly affect the changes in resonant frequency. Although the surface roughness of the Al_2O_3- and Li-coated electrodes may not be identical, a flat surface was assumed for both to simplify the analysis. Consequently, the mass changes can be rationally derived from the observed frequency changes. Upon the first TMA exposure, the Li-coated electrode exhibited a mass gain

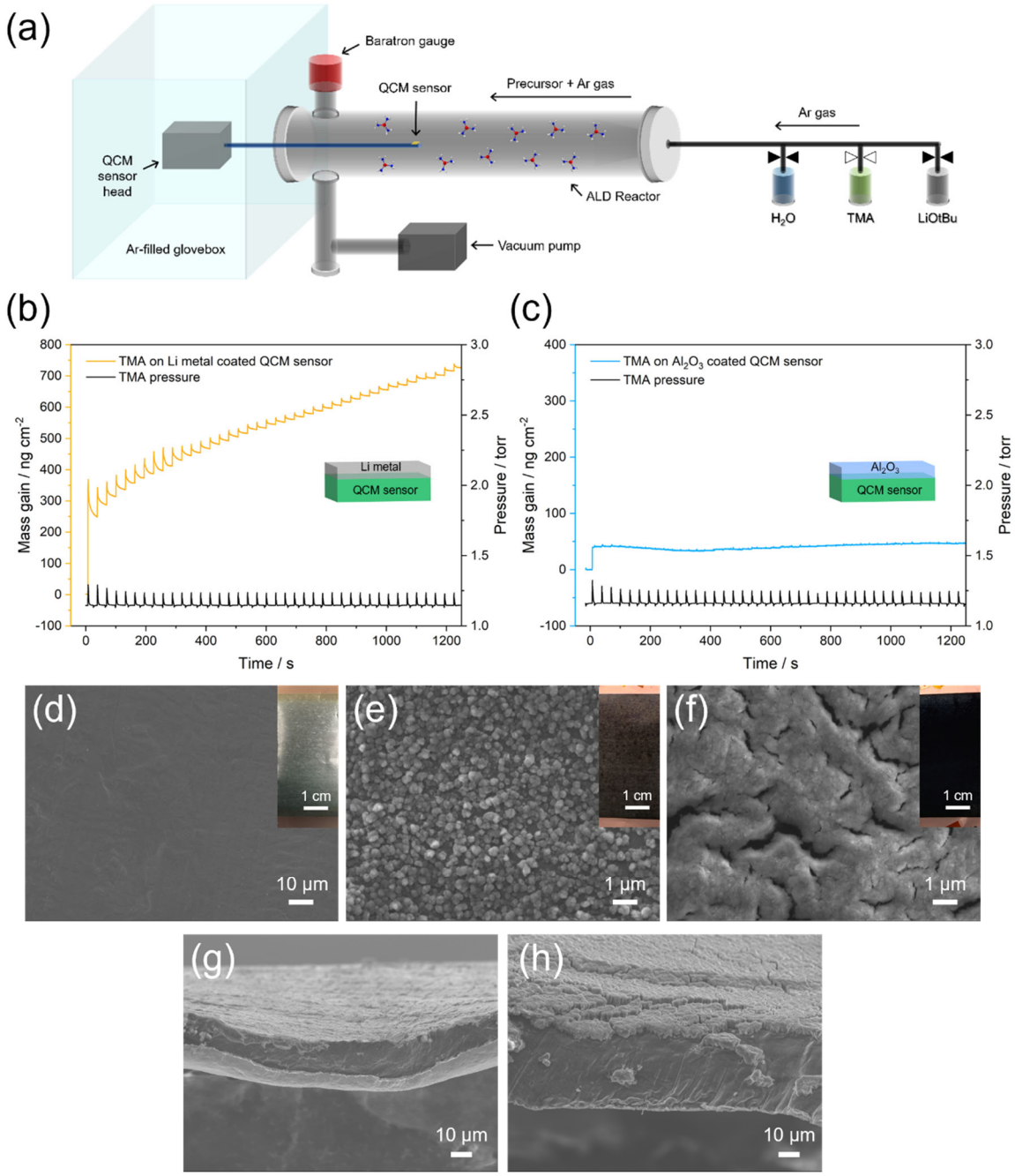

Figure 1. (a) Schematic illustration of ALD reactor with *in situ* QCM connected to Ar-filled glovebox. Mass gain and pressure changes from CVT with TMA on (b) Li metal and (c) Al_2O_3 coated QCM sensor over 40 TMA exposures. SEM images of (d) TMA-20s on Al_2O_3 ALD Li metal electrodes after 50 cycles of TMA/H_2O, (e) TMA-5s on Li, and (f) TMA-20s on Li, with corresponding optical images in the insets. Cross-sectional SEM images of Li metal electrodes for (g) TMA-5s, and (h) TMA-20s.

of ~370 ng cm^{-2}, which is approximately 9.3 times greater than that observed for the Al_2O_3-coated electrode (40 ng cm^{-2}) (Figure 1b, c). This substantial difference indicates that, unlike the predominantly self-limiting chemisorption of TMA on Al_2O_3, Li metal undergoes extensive chemical reactions with the TMA precursor. Moreover, the mass of the Li-coated sensor continued to increase with subsequent TMA exposures, whereas the mass of the Al_2O_3-coated sensor remained constant at the value observed after the initial TMA dosing. This suggests that the CVT process on Li metal is not confined to surface-limited reactions but also involves bulk chemical transformations. In contrast, 40 consecutive TMA exposures on the Al_2O_3 surface keeps the same mass gain of 40 ng cm^{-2}, corresponding to ~1 Å of Al_2O_3 [25], consistent with a self-limiting, surface chemical reaction characteristic of ALD processes.

Figures 1d and e-f show FE-SEM images of the Li surfaces illustrating the morphological changes after TMA CVT on both Al_2O_3-coated and bare Li metal. The Al_2O_3 coating on Li metal was accomplished using 50 TMA/H_2O ALD cycles with 1 second precursor exposures, producing a uniform surface comparable to that of the pristine Li metal (Figure S1). After 20 seconds of TMA CVT on the Al_2O_3 ALD Li, no noticeable morphological changes are observed compared to its pre-CVT state (Figure 1d). In contrast, TMA CVT on the bare Li for 5 seconds (TMA-5s) led to the formation of dense spherical morphology, several hundred nanometers in diameter, on the Li metal surface (Figure 1e). With extended TMA CVT time for 20 seconds (TMA-20s), spherical morphology further evolved into a continuous, flat, and dense layer, visually appearing darker black on the Li metal surface (Figure 1f and Figure S2). Notably, EDS elemental mapping showed a low Al content of ≈5.4 % for the Al_2O_3 ALD Li metal, whereas the Al content significantly increased to ≈21.1 % on bare Li subjected to the same TMA CVT for 20 seconds (Figure S3). This substantial increase indicates that the CVT process induces extensive chemical reactions

between Li metal and TMA leading to pronounced morphological changes on the order of hundreds of nanometers and a final composition that is strongly dependent on the duration of TMA exposure. In addition, cross sectional SEM images of Li metal anodes after TMA CVT times of 5 and 20 seconds show uniform layers of approximately 800 nm and 2 μm thickness, respectively (Figures 1g, h). It is notable that the lower mass gain observed in QCM, despite the substantial structural changes seen in SEM, can be attributed to differences in Li film morphology, specifically the porosity and reduced density of e-beam-evaporated Li relative to roll-pressed Li foils, as well as the contribution of low-density species within the CVT-formed SEI layer. These combined factors reconcile the discrepancy between the nanogram-scale mass change and the micron-scale morphological evolution.

2.2 Analysis of SEI following CVT on Li metal

To investigate the role of CVT in modifying the SEI layers on the Li surface, we performed XPS measurements to compare the composition of the SEI layers on bare Li, TMA-5s, and TMA-20s. **Figure 2** shows high resolution C 1s, O 1s, Al 2p, and Li 1s XPS spectra of the SEI layers formed on bare Li and following 5s and 20s CVT. Corresponding survey spectrums were also shown in **Figure S4**. On bare Li, the native passivation layer is generally dominated by Li_2CO_3 and Li_2O. Although LiOH may form transiently, it readily converts to Li_2O or Li_2CO_3 upon exposure to trace O_2 or CO_2. For this reason, LiOH was not considered a major component of the native passivation layer. The surface Li_2CO_3 impurity is characterized by a O–C=O peak at 288.5 eV in the C 1s,[26] 531 eV in the O 1s, and 55.0 eV in the Li 1s XPS spectra (Figure 2a, d, j). Li_2O is identified by peaks at approximately 528.3 eV in the O 1s and 53.8 eV in Li 1s XPS spectra (Figure 2d, j).[27] In contrast, the intensities of the corresponding peaks were significantly reduced in TMA- 5s and

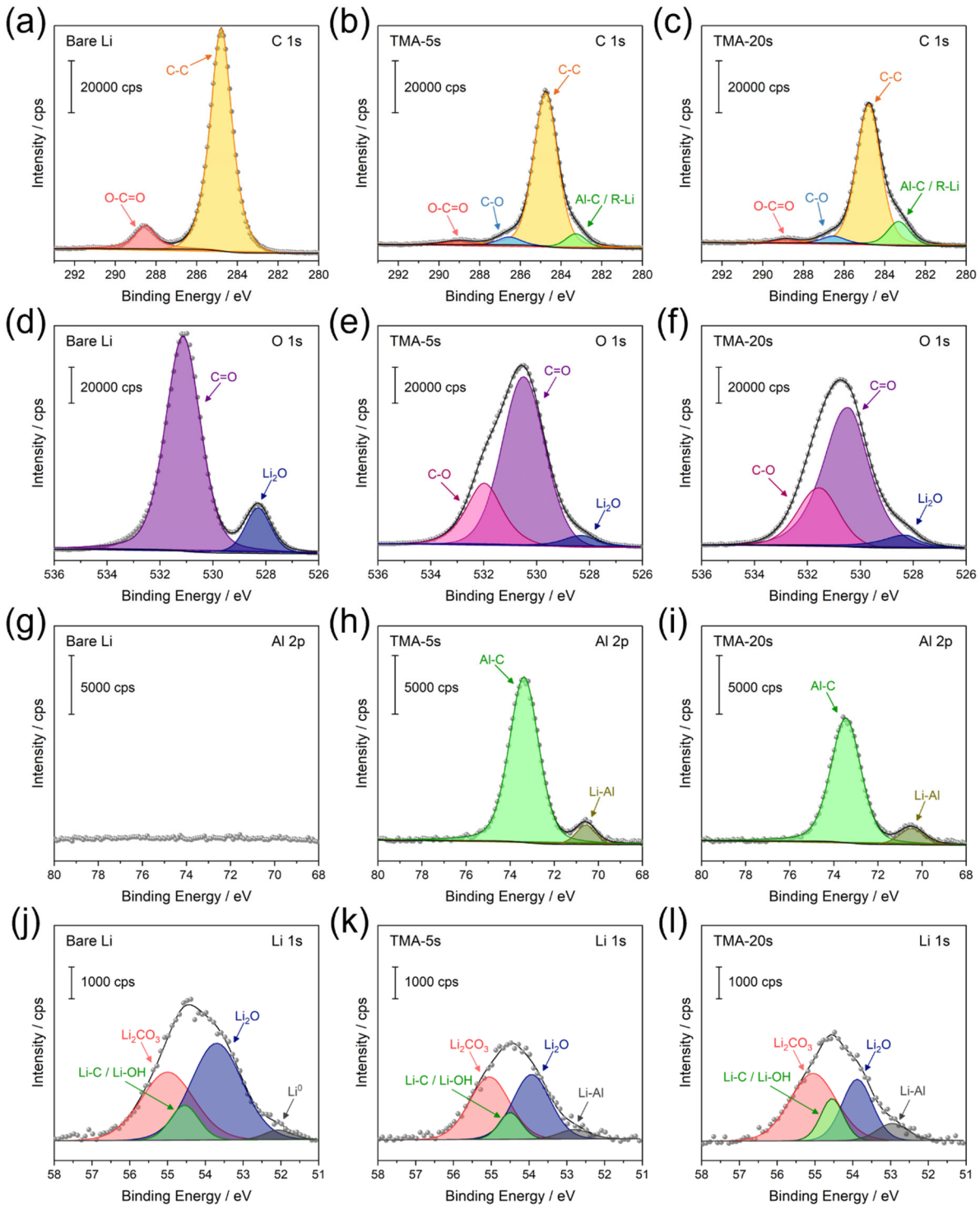

Figure 2. (a-c) C 1s, (d-f) O 1s, (g-i) Al 2p, and (j-l) Li 1s XPS spectrum for (a, d, g, j) bare Li, (b, e, h, k) TMA-5s, and (c, f, i, l) TMA-20s.

188 TMA-20s, suggesting removal of the surface impurities or modification of the native passivation
189 layer through CVT (Figure 2b, e, k and Figure 2c, f, l). Moreover, new peaks appear after CVT,
190 including R–Li and Al–C peaks at approximately 283.3 eV in the C 1s XPS spectra, as well as Li–
191 Al and Al–C peaks at approximately 70.5 eV and 73.5 eV in the Al 2p XPS spectra (Figure 2a-c,
192 and Figure 2g-i).[28] This implies that Li metal chemically reacted with TMA, leading to the
193 formation of Li–Al, Li–C, and Al–C bonds. Additionally, we suggest that the formation of C–O
194 peaks after CVT primarily originate from surface Li_2CO_3 and Li_2O species, which are
195 progressively transformed and consumed during surface reconstruction and subsequent reactions
196 between Li metal and TMA. Therefore, these signals should not be interpreted as evidence of
197 newly generated compounds but rather as a reflection of the dynamic evolution of pre-existing
198 surface species. The detailed structure of the SEI formed after CVT for 20 seconds was examined
199 using XPS depth profiling measurements (**Figures 3**a-d). For reference, we also performed XPS
200 measurements on a Li-Al alloy sample. In the outermost SEI layer, a strong C–C peak was
201 observed in the C 1s XPS spectrum, while the intensity of the metallic Al and Li–Al peaks in the
202 Al 2p and Li 1s XPS spectra gradually increased with depth into the SEI layer. During sputtering,
203 the Al–C peak in the Al 2p XPS spectrum initially increased and then decreased and disappeared
204 by 1500 s, whereas the Al–C/R–Li peak in the C 1s XPS spectrum increased and remained strong
205 until 6000 s. This suggests that R–Li extends much deeper below the SEI surface compared to Al–
206 C. Therefore, TMA CVT facilitates SEI formation, with an inner layer composed of metallic Al,
207 Li–Al and R–Li, a middle layer composed of Al–C, and an outermost layer of carbonaceous
208 compounds. To further elucidate the composition of the carbonaceous layers on the Li surface after
209 CVT, we conducted UV Raman spectroscopy (Figure 3e). The TMA-20s sample was loaded into
210 an air-tight Raman cell inside the Ar-filled glovebox followed by air-free transfer into the Raman

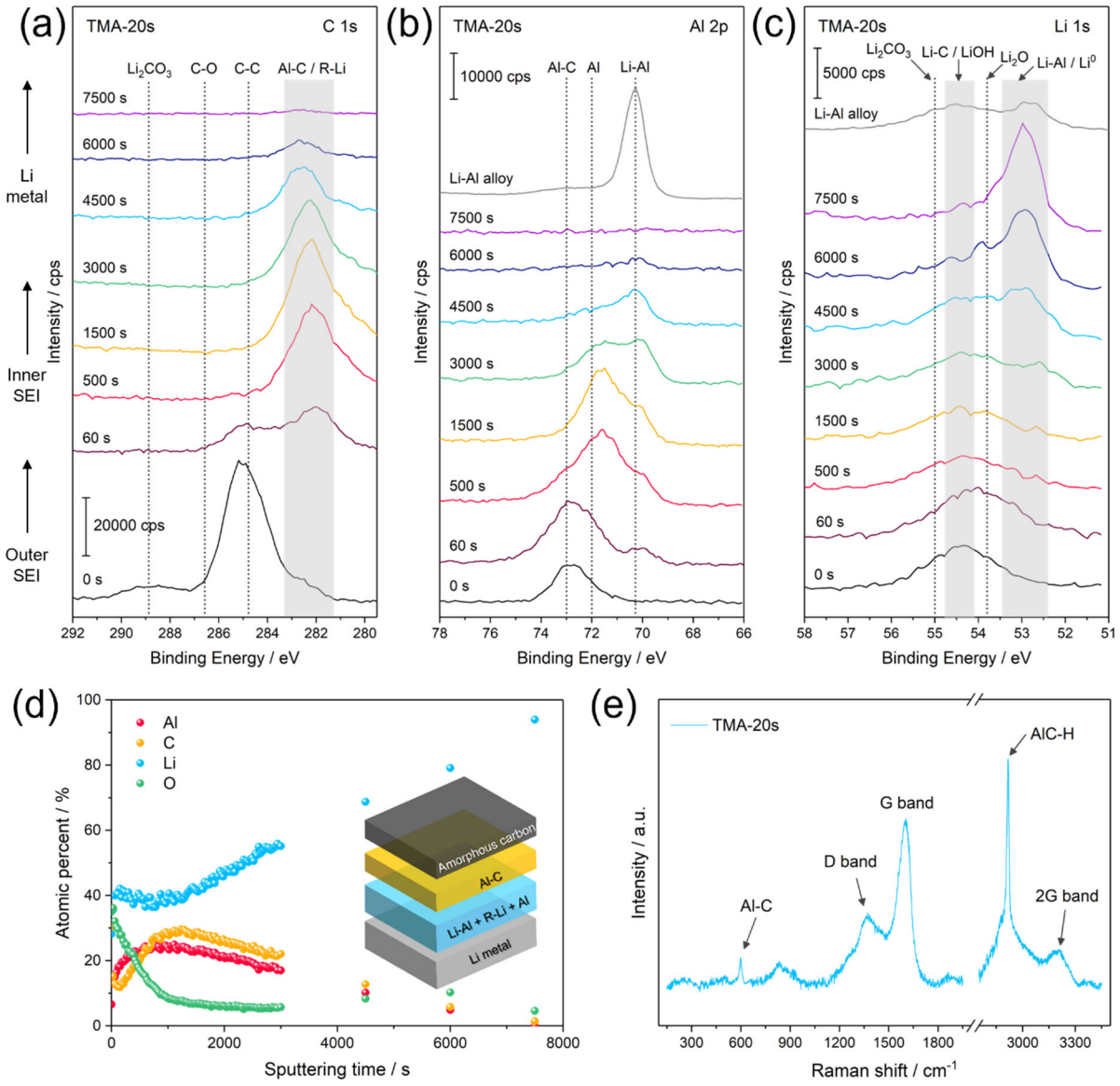

Figure 3. (a) C 1s, (b) Al 2p, (c) Li 1s, and (d) atomic ratio depth profiles from XPS spectrum of TMA-20s and Li–Al alloy reference sample. Inset schematic in (d) shows the SEI structure formed on Li after CVT. (e) UV Raman spectrum of TMA-20s.

spectrometer where analysis was performed under a continuous helium flow. The Raman peaks observed at approximately at 1370 cm^{-1} and 1590 cm^{-1} corresponding to the D and G bands, respectively. This indicates that the carbonaceous SEI layer on the Li surface is predominantly disordered, which aligns well with the characteristic spectrum of amorphous carbon.[29,30] Additionally, distinct peaks at 598 cm^{-1} and 2917 cm^{-1}, corresponding to Al–C and AlC–H vibrations, respectively, were clearly identified by UV Raman spectroscopy, further supporting the formation of Al–C species on the Li metal surface. The binding energies of the XPS peaks and their corresponding references are provided in Table S1.

2.3 Reaction mechanism of TMA CVT on Li and native SEI

Previous studies of TMA thermal decomposition may be insightful as they refer to compounds that we have identified in our XPS analysis. For instance, Zhang et al. reported that TMA undergoes thermal decomposition at temperatures below 500 °C resulting in the formation of Al–C–Al–C compounds.[31] At significantly higher temperatures (950–1100 °C), pyrolysis of TMA has been shown to produce aluminum carbide powders.[32] Other studies have demonstrated the decomposition of TMA on heated metal and Si(100) surfaces at temperatures up to 900 K revealing the formation of Al–Al bonds and carbonaceous species indicative of Al-C bond cleavage.[33] While the exact reaction pathways between TMA and Li metal differ from these thermal processes, our work suggests that fresh Li metal catalyzes a similar decomposition behavior, resulting in the deposition of the metallic Al, Al–C, and amorphous carbon composite on the Li surface. The high reactivity of TMA is attributed to its electron-deficient aluminum center[33] which readily accepts electrons from donor species. In this study, Li metal appears to act as an electron donor facilitating the decomposition of TMA and enabling surface modification via catalytic reaction pathways.[34]

To understand the reaction mechanism of TMA CVT on Li metal and its native passivation layer, we conducted computational studies based on density functional theory (DFT) calculations of TMA reaction on three different surfaces: Li, Li_2O, and Li_2CO_3. The most commonly observed and stable surfaces: the (110) surface for Li,[35,36] the (111) surface for Li_2O,[37-40] and the (001) surface for Li_2CO_3[41-43] were selected. Figure 4 shows energy profiles for the stepwise demethylation reaction of TMA on the Li (110) surface along two different pathways, with insets showing the optimized geometries at each reaction step. The demethylation reaction of TMA can be represented as follows:

$$\mathrm{TMA\ (g)} + * \rightarrow \mathrm{TMA}^* \qquad (2)$$

$$\mathrm{TMA}^* + * \rightarrow \mathrm{DMA}^* + \mathrm{CH_3}^* \qquad (3)$$

$$\mathrm{DMA}^* + * \rightarrow \mathrm{MA}^* + \mathrm{CH_3}^* \qquad (4)$$

$$\mathrm{MA}^* + * \rightarrow \mathrm{Al}^* + \mathrm{CH_3}^* \qquad (5)$$

where * represents the surface, DMA^* is $Al(CH_3)_2{}^*$, and MA^* is $AlCH_3{}^*$. In both pathways, the relative energy values are reference to step (2) which corresponds to gas phase TMA and the Li surface. The adsorption of TMA (TMA^*) results in a substantial energy stabilization of –1.3 eV, indicating a strong interaction between TMA and the Li surface. Figure 4a shows the stepwise demethylation pathway, ultimately leading to the formation of Al^* with a relative energy of –2.2 eV. This pathway suggests a relatively direct and thermodynamically favorable decomposition process where the Al atom remains on the top layer of the Li surface. Moreover, Figure 4b shows a different decomposition pathway in which demethylation is accompanied by a structural rearrangement of the Li surface. In both cases, all atomic positions were fully relaxed (with the lower Li layers constrained as described in the Methods), and the "without rearrangement" condition in Figure 4a corresponds to a local minimum where Al remains on the top of the lattice.

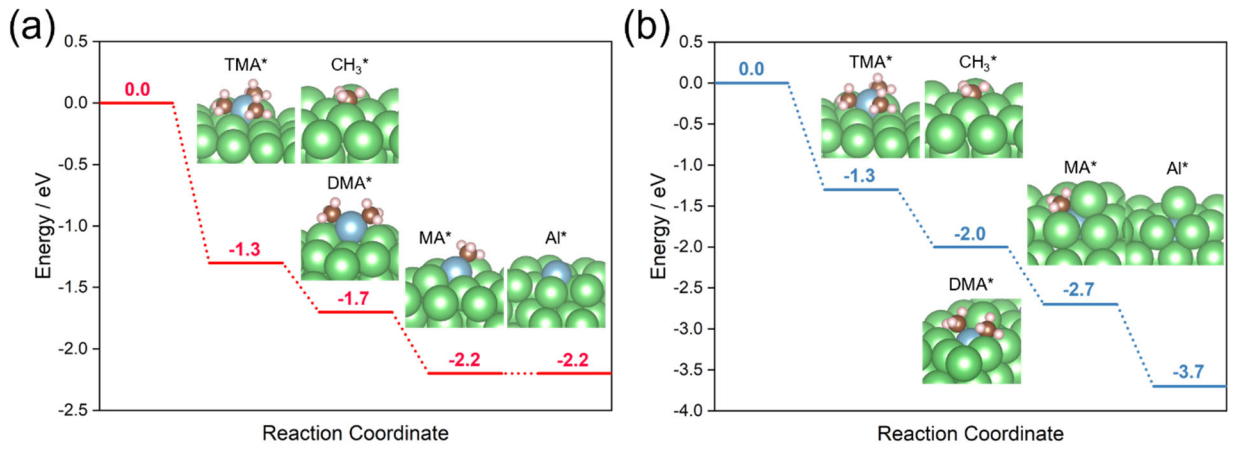

Figure 4. Energy profiles for TMA reaction via demethylation (a) on the Li surface and (b) on the Li surface with subsequent rearrangement. Insets present optimized geometries (green: Li, light blue: Al, dark brown: C, and white: H).

For both cases, multiple adsorption configurations of TMA and CH_3* were investigated, and only the most stable states are reported. This pathway demonstrates that demethylation proceeds with thermodynamic stabilization, ultimately reaching a final state with an energy of –3.7 eV. The rearrangement involves Al displacing Li atoms from the top layer thereby modifying the local electronic structure and coordination environment. Consequently, the Li–Al rearrangement explains why the reaction extends beyond the surface and progresses into the bulk as the CVT time increases (Figures 1b, c). The insets in Figure 4 show the evolving surface configurations illustrating how Al^* and CH_3^* interact with the Li substrate at each stage. This comparison between the two pathways highlights the role of surface structure and coordination effects in determining the stability and reactivity of TMA-derived intermediates on the Li surface. Furthermore, the observed energetically favorable bonding between Li–Al and Li–C is further supported by the XPS and Raman results presented in Figures 2 and 3. While TMA preferentially adsorbs on Li_2O and Li_2CO_3 surfaces, its demethylation is not thermodynamically favorable (Figure S5 and S6). However, due to the electron deficient nature of the Al atom in TMA, Li atoms beneath the thin

Li_2O or Li_2CO_3 layer may function as catalysts for structural rearrangement between adsorbed Al atoms, thereby facilitating the removal of the native SEI layer on the Li surface (Figure 2 and 3).

During the formation of MA^* via the removal of two methyl groups, there is a possibility of C_2H_6 gas generation through the coupling of two CH_3^* species. On the Li surface without surface structural rearrangement (Figure 4a), the relative energy of C_2H_6 formation with MA^* is calculated to be –0.8 eV, which is higher than that of MA^* with two CH_3^* species at –2.2 eV. Similarly, when Li surface rearrangement is considered (Figure 4b), the energy of C_2H_6 formation from TMA is –1.4 eV, which remains higher than the MA^* intermediate with CH_3^* at –2.7 eV. This suggests that methyl groups are more likely to remain adsorbed on the Li surface rather than desorbing as ethane. However, in the CVT setup where a constant flow of Ar carrier gas is maintained, any ethane product would be swept away from the surface, thereby shifting the equilibrium towards ethane formation. In contrast, on the Li_2O and Li_2CO_3 surfaces, the relative formation energies for C_2H_6 are calculated to be 0.14 eV and 0.97 eV, respectively, both lower than those of the corresponding MA^* intermediates with two CH_3^* groups. Nevertheless, the overall process, including ethane release and TMA demethylation, remains thermodynamically unfavorable due to the relatively stronger adsorption of TMA on these oxidized surfaces.

To further investigate potential gaseous reaction byproducts generated during CVT, we performed *in situ* QMS measurements with 10 sequential, 5 s TMA exposures separated by 15 s purge periods in a reactor containing Li metal (Figure S7). We also performed a background measurement under the same TMA dosing conditions but without Li metal in the reactor (Figure S8). For the empty reactor, we observed peaks corresponding to CH_3^+ (m/z = 15) , and $Al(CH_3)_2^+$ (m/z = 57), both of which are fragments of the parent TMA compound.[44] A small peak at m/z = 29 is expected based on the TMA cracking pattern,[44] but we do not observe distinct m/z = 29

signals during the TMA dosing in our background measurement (Figure S8). Although we observe an increase in the m/z = 29 noise floor that correlates with the TMA dosing, the signals are actually lower when the TMA valve is opened so we believe this is an artifact. During the *in situ* QMS measurements with the Li metal anodes installed in the reactor, we observe the same TMA fragments at m/z = 15 and m/z = 57, but a new peak appears at m/z = 29, followed by the TMA dose, that we attribute to $C_2H_5^+$, a fragment of ethane [NIST database]. The persistence of this peak over multiple TMA exposures suggests that this is not the result of a self-limiting surface reaction but rather forms continuously during the CVT reaction of TMA with Li metal. Although the DFT calculations predict that MA^* is more stable compared to C_2H_6, ethane formation also has a negative free energy, and our QMS measurements indicate that some ethane is produced during CVT and is transported away from the Li surface by the carrier gas flow.

2.4 Electrochemical performance of TMA CVT on Li

The CVT-derived SEI layer described above is composed of metal-carbon composite layers and Li–Al alloy phases. This unique SEI composition could be beneficial for enhancing electrochemical performance in batteries, given that metal-carbon composite anodes have previously demonstrated excellent electrochemical behavior.[45,46] To evaluate this hypothesis, we conducted a series of electrochemical measurements using various testing methodologies. Figure 5a shows the voltage profiles of Li electroplating on bare Li, TMA-5s, TMA-10s, and TMA-20s using 1.2 M $LiPF_6$ in EC/EMC (3/7, w/w) electrolyte at a current density of 0.5 mA cm^{-2}. When CVT was applied for 5–10 seconds, the nucleation overpotential decreased to less than half of that observed for bare Li. However, extending the CVT time to 20 seconds resulted in the nucleation overpotential exceeding that of bare Li. This facile Li nucleation on TMA-5s might be attributed

to the spherical morphology formed on the Li surface which serve as effective nucleation sites. We also measured the exchange current density for bare Li, TMA-5s, TMA-10s, and TMA-20s (Figure 5b). The exchange current density was calculated from the Tafel plot in the high overpotential region (> 118 mV at 25 °C) at a scan rate of 1 mV s^{-1} (Figure S9). Interestingly, the exchange current density (i_0) increased with increasing nucleation overpotential (η), implying that Li nucleation becomes more facile as the exchange current density decreases under the same electrolyte conditions. The correlation between η and i_0 can also be explained by the Tafel equation (6) and the Gibbs free energy of nucleation (7), as shown below:[47,48]

$$\log\left(\frac{|i|}{i_0}\right) = \frac{\alpha F|\eta|}{2.3RT} = \mathrm{A}|\eta| \qquad (6)$$

$$\Delta G_{nucleation} = \frac{2\pi r^3 nF|\eta|}{3V_m} + 2\pi r^2\sigma = \mathrm{B}|\eta| + \mathrm{C}\sigma \qquad (7)$$

where R is the gas constant, T is the temperature, F is the Faraday`s constant, r is the radius of the semi-sphere morphology, V_m is the molar volume of Li, α is the transfer coefficient, and σ is the surface tension between Li and the electrolyte. By combining equations (6) and (7), the nucleation process of Li on different substrates is not only related to η but also to i_0.

Next, we compared the electrochemical performance of TMA CVT 20 μm Li with a sulfide solid-state electrolyte (LPSCl) and a carbonate electrolyte (1.2 M $LiPF_6$ in EC/DMC (3/7, w/w)). **Figure 5**c shows the voltage profiles of Li|Li symmetric cells with the conventional carbonate electrolyte at an areal capacity of 0.2 mA h cm^{-2} and a current density of 0.2 mA cm^{-2}. TMA-5s exhibited stable cycle performance over 300 hours maintaining a constant overpotential below 0.05 V during extended cycles (Figure S10). With increasing CVT time beyond 5 seconds, cycle performance gradually decreased, and for TMA-20s, cyclability was even lower than that of bare Li. Figure 5d shows the Nyquist plots of Li|Li symmetric cells with a carbonate electrolyte after 3

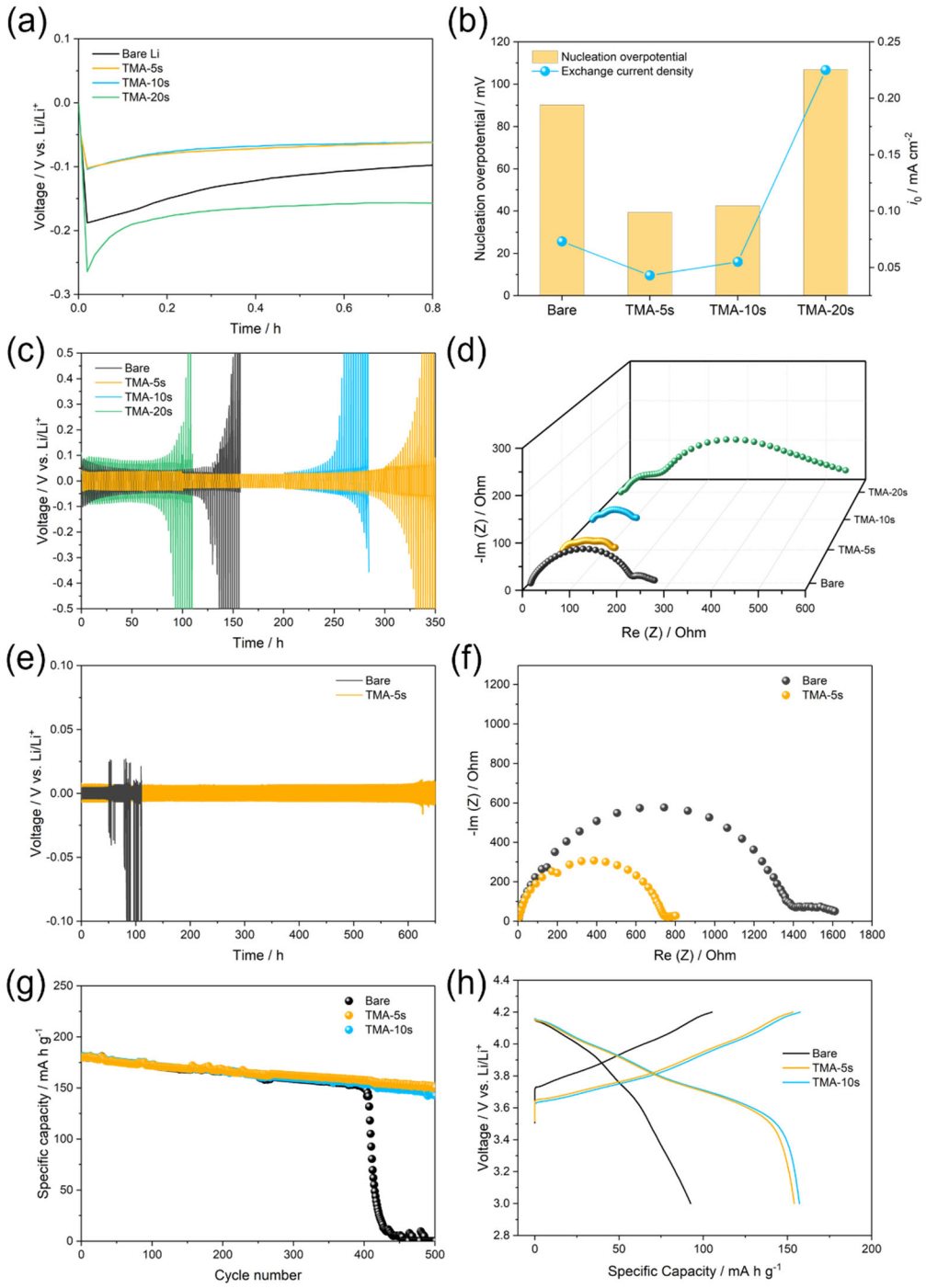

Figure 5. (a) Nucleation overpotential of bare Li, TMA-5s, TMA-10s, and TMA-20s at 0.5 mA cm^{-2}, and (b) the corresponding exchange current density from the fitted Tafel curves at a scan rate of 1 mV s^{-1}. (c) Voltage profiles and (d) Nyquist plots of 20 µm Li|20 µm Li symmetric cells after various times of TMA CVT on Li. Voltage profiles were obtained with an areal capacity of 0.2 mA h cm^{-2} at a current density of 0.2 mA^{-2}, using 1.2 M $LiPF_6$ in EC/DMC (3/7) as an electrolyte. (e) Voltage profiles and (f) Nyquist plots of 20 µm Li|LPSCl|20 µm Li and TMA-5s|LPSCl|TMA-5s cells with an areal capacity of 0.2 mA h cm^{-2} at a current density of 0.2 mA^{-2}. (g) Cycle performance and (h) corresponding voltage profiles of NMC 811 with 20 µm Li, TMA-5s, and TMA-10s using 1.2 M $LiPF_6$ in EC/DMC (3/7) + 5 wt% FEC as the electrolyte.

days of rest at room temperature. The semicircle size, representing the sum of SEI and charge transfer resistance, gradually increased with longer CVT times exhibiting the same trend as the cycle performance. This is attributed to the fact that spherical morphology formed on the Li surface were excessively thickened by the amorphous carbon layer which leads to an increase in interfacial resistance hindering Li^+ transport when CVT is conducted for more than 5 seconds. Figure 5e shows the voltage profiles of Li|LPSCl|Li cells at an areal capacity of 0.2 mA h cm^{-2} and a current density of 0.2 mA cm^{-2}. TMA-5s exhibited uniform plating and stripping with a constant overpotential for over 300 cycles, lasting approximately 7 times longer than bare Li at room temperature. This significant improvement in cyclability can be attributed to the multilayered SEI formed after TMA CVT consists of distinct functional layers, each serving a unique role at the interface between the sulfide solid-state electrolytes (SSEs) and Li metal. The innermost Li-Al alloy-based SEI layer can mitigate volume expansion and serve as lithiophilic nucleation sites,[49,50] while the outermost amorphous carbon layer facilitates Li^+ transport through pathway channels resulting in lower interfacial resistance and enhanced wettability.[51-53] Nyquist plots collected before cycling also revealed that the interfacial resistance at the TMA-5s-LPSCl interface was nearly half of that at the Li-LPSCl interface (Figure 5f). Figure 5g shows the cycle performance of 20 μm Li | NMC811 with carbonate electrolyte with 5 wt% FEC additives for bare Li, TMA-5s, and TMA-10s at a C/3 rate. Figure 5h shows the corresponding voltage profiles for 20 μm Li | NMC811 cells after 410 charge-discharge cycles. TMA-5s demonstrated stable cycling for 500 cycles whereas bare Li showed discharge capacity fading after 400 cycles. These results clearly demonstrate that TMA CVT Li exhibits excellent stability with SSEs and carbonate electrolytes compared to bare Li owing to its multifunctional SEI layer.

Figure 6 shows a comparative schematic of the CVT process and the conventional ALD process on Li metal anodes. In Al_2O_3 ALD, TMA and H_2O are alternatively introduced and the TMA reacts with surface –OH groups formed by H_2O exposure on the native passivation layer to enable layer-by-layer growth. In contrast, the CVT process exhibits a distinctive mechanism. When TMA is dosed for a short time (1 second), no appreciable reaction is observed (Figure S11). However, with extended exposure (≥ 5 seconds), the native passivation layer on the Li surface is gradually removed allowing TMA to chemically transform the Li metal to form a robust, multi-layer SEI architecture. This architecture consists of spherical morphology with a Li–Al alloy in the inner region and amorphous carbon on the surface. The resulting structure exhibits excellent stability against both SSEs and carbonate-based liquid electrolytes. It is somewhat surprising that the CVT process has not been reported in previous studies of Al_2O_3 ALD on Li metal anodes.[13-15] This may be attributed to insufficient TMA exposure in previous studies or to the presence of a thick native passivation layer that hindered chemical interaction between TMA and Li. Indeed, when we performed CVT using lithium with a heavily passivated surface, no noticeable color change occurred but the Li_2CO_3 peak signal decreased in C 1s XPS spectra. However, after mechanically polishing the surface to remove the passivation layer, the Li foil immediately reacted with TMA within one second (Figure S12). In addition, once 50 TMA/H_2O ALD cycles of the conventional Al_2O_3 ALD process are completed, the resulting layer effectively inhibits the CVT process, as demonstrated in Figure 1d.

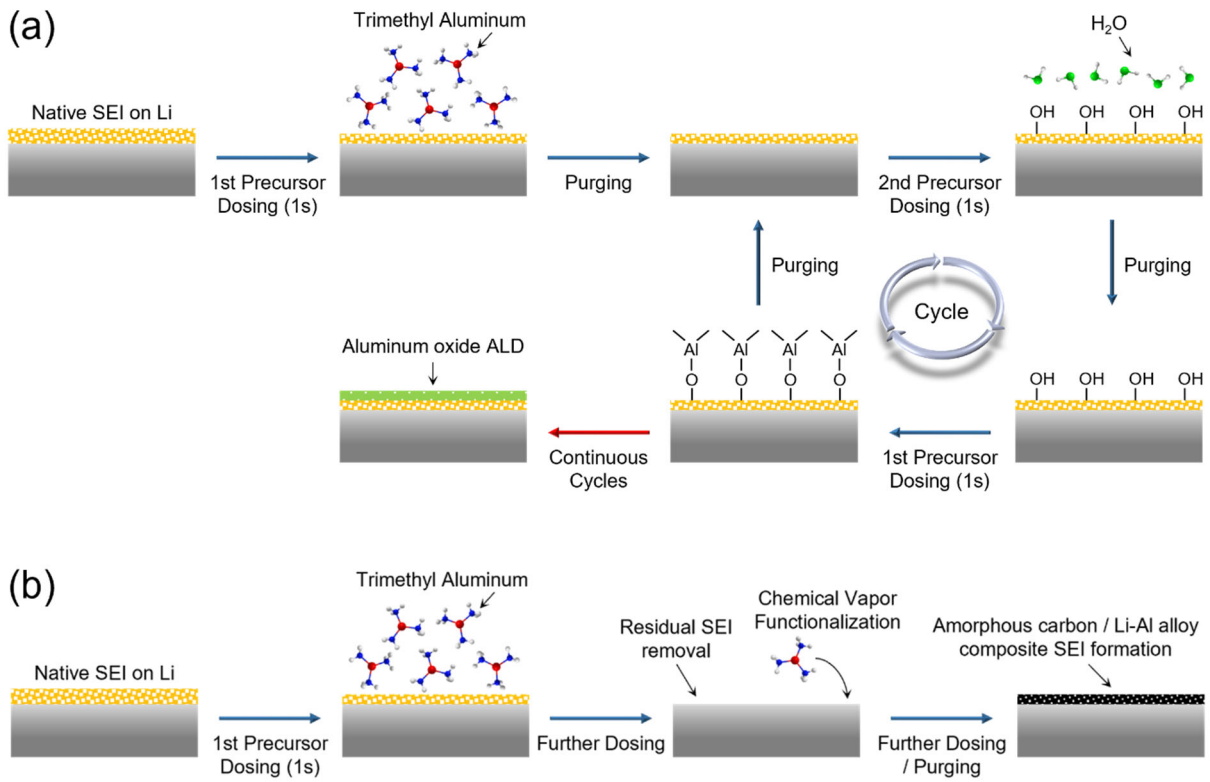

399

400 **Figure 6**. Schematic illustration of the (a) atomic layer deposition (ALD) process for aluminum oxide and the (b)
401 chemical vapor transformation (CVT) mechanism of the TMA precursor on the Li metal anode.

3. CONCLUSIONS

In this study, we demonstrated the chemical vapor transformation (CVT) mechanism of trimethylaluminum (TMA) on Li metal anodes providing insights into the interfacial modification of Li metal anodes for high energy density batteries. Unlike conventional atomic layer deposition (ALD), the CVT process on Li metal exhibits a distinct reaction behavior due to the presence of native passivation layers and the intrinsic chemical reactivity of Li metal. Through *in situ* QCM and QMS, *ex situ* XPS and UV Raman spectroscopy, and DFT calculations, we elucidated how TMA interacts with both the native SEI and bare Li forming a multilayer SEI structure with a Li-Al alloy at the inner interface and amorphous carbon at the outer surface. Taken together, the QCM mass evolution, depth-resolved XPS, SEM cross-sections, and DFT calculations support a subsurface-assisted mechanism in which TMA initially reacts with thin or defective regions of Li_2O/Li_2CO_3, enabling access to the underlying Li metal. Subsurface Li atoms subsequently promote Al insertion and methyl-group cleavage, lowering the reaction barrier and facilitating progressive removal of the native passivation layer. As a result, a chemically graded interphase forms, with an outer amorphous carbon layer, a mid-region containing Al–C species, and an inner Li–Al alloy layer. The continuous, non-self-limiting mass increase observed in QCM, and the large-scale structural reconstruction seen in SEM, are fully consistent with this mechanism. Electrochemical evaluation confirmed that Li metal treated with TMA for 5 seconds (TMA-5s) exhibited significantly enhanced cycling performance in both sulfide solid-state electrolytes (SSEs) and carbonate electrolytes. Notably, the TMA-5s|LPSCl|TMA-5s cell achieved a cycle life up to seven times longer than bare Li, while TMA-5s|1.2 M $LiPF_6$ in EC/EMC|TMA-5s demonstrated more than double the cycling stability. These improvements are attributed to the lithiophilic Li-Al alloy layer which enhances interfacial stability and the amorphous carbon layer

that facilitates Li^+ transport. However, excessive CVT exposure beyond 5 seconds led to increased interfacial resistance underscoring the importance of optimizing CVT conditions for practical applications. Overall, our findings highlight CVT as a scalable and efficient method for enhancing the stability and electrochemical performance of thin Li metal anodes, given the total reaction times of just a few seconds. The ability to rapidly functionalize Li surfaces in a single step opens new pathways for advancing next-generation Li metal batteries, including all-solid-state batteries, by mitigating key interfacial challenges.

EXPERIMENTAL PROCEDURES

ALD and CVT of Li metal: ALD and CVT were performed in a custom viscous flow stainless steel tube reactor system connected to a glovebox, using Ar (UHP, 99.999 %) as the carrier gas at a flow rate of 40 sccm, 150 °C, and a pressure of approximately 1.2 Torr.[54,55] Al_2O_3 ALD was conducted by alternating exposures to TMA and H_2O, with each precursor dosed for 1 s, followed by a 15 s purge. TMA CVT was conducted by exposures to TMA for 5, 10, 20 s, followed by a 15 s purge.

Materials: 1.2 M $LiPF_6$ in EC/EMC (3/7, w/w) with or without 5 wt% of FEC was used as liquid electrolyte. 20 μm Li metal foil was purchased from Honjo Metal, Japan. Commercial LPSCl powder was received from NEI, USA. $LiNi_{0.8}Mn_{0.1}Co_{0.1}O_2$ was purchased from MTI corporation. For the preparation of $LiNi_{0.8}Mn_{0.1}Co_{0.1}O_2$ electrodes, active materials were mixed with carbon black (Super P) and polyvinylidene fluoride (PVdF) in a weight ratio of 8:1:1. The slurry in N-methyl-2-pyrrolidone (NMP) solvent was casted onto an Al foil current collector. Electrodes were dried under vacuum overnight at 120 °C before use.

Materials Characterization: In situ quartz crystal microbalance (QCM) measurements were conducted using modified quartz crystals installed in a QCM holder (Maxtek BSH-150 bakeable sensor head). CVT was conducted by dosing multiple times of TMA for 2 seconds followed by a 30 second purge. Prior to CVT, the QCM signal was stabilized inside the ALD reactor at 150 °C. The modified quartz crystals were prepared by depositing approximately 10 nm of Al_2O_3 and 500 nm of Li metal, respectively. Electron beam (e-beam) deposition of Li metal thin films was performed in a UHV chamber (base pressure 5×10^{-10} mbar) with direct connection to an Ar atmosphere glove box. E-beam evaporation was performed using a 5 kV accelerating voltage and 3 mA emission current at a source-to-substrate distance of ca. 50 cm. Background pressure was $\leq 5 \times 10^{-7}$ mbar throughout e-beam deposition. *In situ* quadrupole mass spectrometry (QMS) measurements (Stanford Research Systems, Model RGA300) were performed in the downstream region of the reactor within a differentially pumped chamber, separated from the reactor tube by a 35 μm orifice. This setup maintained an approximate pressure of 10^{-6} Torr in the QMS chamber. Gas-phase products generated during the CVT could pass through the orifice and be detected by the QMS, which was interfaced with a PC for data recording. UV Raman spectroscopy was employed to probe the chemical information of the surface of the samples. The laser excitation wavelength of 375 nm was provided by the second harmonic generation output of 750 nm laser line from a 4 kHz repetition rate, nanosecond pulsed, wavelength-tunable Ti:Sapphire laser (Coherent, Indigo-S). A collimated laser light was focused onto the sample, and the scattered light from the sample refocused with a home-made 90° off-axis ellipsoidal reflector with the backscattering geometry to a triple-grating spectrometer (Princeton Instruments, Trivista 555) where Rayleigh light was filtered out and stray light significantly suppressed.[56] The Raman light was collected by a UV-enhanced liquid nitrogen cooled CCD detector (Princeton Instruments,

SPEC-10). To avoid possible laser-induced degradation of samples during Raman measurements, low laser powers were delivered on the sample (typically 1 mW). All Raman spectrum of the samples were obtained in flowing helium (~100 mL min^{-1}) at room temperature using *in situ* Raman cell (Harrick Scientific). A field emission scanning electron microscope (FE-SEM, JEOL IT800HL, Japan) was performed in the Center for Nanoscale Materials (CNM) at Argonne to obtain scanning electron microscopy (SEM) and energy-dispersive spectrometry (EDS) mapping images. X-ray photoelectron spectroscopy (XPS) was performed in an UHV operating at base pressures of 10^{-9} mbar (Thermo Scientific, ESCALAB 250Xi) with a nominal spot size of 400 μm and pass energy of 50 eV. A depth profile for each element was calculated from the integrated peak intensity and an ionization constant for each element. The estimated etching rate process was 0.19 nm s^{-1}, based on Ta_2O_5 as a reference. Binding energies were calibrated with respect to the adventitious carbon C 1s peak at 284.8 eV.

Electrochemical Measurements: Li|Li symmetric cells and Li|$LiNi_{0.8}Mn_{0.1}Co_{0.1}O_2$ cells were assembled using 2032-type coin cells, with 20 μm Li metal foil used in all experiments. The cycle performance of Li|Li symmetric cells was evaluated with Arbin BT-2043 battery cycler at room temperature. The cycle performance of Li|$LiNi_{0.8}Mn_{0.1}Co_{0.1}O_2$ cells was evaluated using a Macor battery cycler in the voltage range of 3.0–4.3 V (vs. Li/Li^+) at 30 °C. The 1 C rate for $LiNi_{0.8}Mn_{0.1}Co_{0.1}O_2$ was equivalent to 180 mA h g^{-1}, with a mass loading of approximately 2.5 mg cm^{-2}. A bulk-type Li|Li_6PS_5Cl|Li cell was fabricated using a trilayer structure consisting of two 20 μm Li metal foils and a solid electrolyte pellet. The solid electrolyte layer was first pelletized at 150 MPa, forming pellets with a diameter of 10 mm and a thickness of approximately 500 μm. Subsequently, Li metal foils were attached to both sides of the solid electrolyte pellet. The Tafel plots of Li|Li cells were obtained at a scan rate of 1 mV s^{-1}. Electrochemical impedance

493 spectroscopy (EIS) was performed using an SP-300 potentiostat (Biologic, France) in a frequency
494 range from 1 MHz to 10 mHz with a potential amplitude of 10 mV.

495 *Computational Methods:* All computations were conducted using spin-polarized density
496 functional theory (DFT) methods. Surface system calculations were performed with the Vienna
497 Ab initio Simulation Package (VASP) employing the projector augmented wave (PAW) method.
498 The electron-exchange correlation energy was described using the strongly constrained and
499 appropriately normed (SCAN) meta-generalized gradient approximation (meta-GGA) functional.
500 Three different surfaces were obtained based on the bulk structures: Li ($Im\bar{3}m$), Li_2O ($Fm\bar{3}m$),
501 and Li_2CO_3 (C/2c). All bulk structures were optimized using a plane-wave cutoff energy of 550
502 eV and a 6 × 6 × 6 k-point mesh within the Monkhorst-Pack scheme, ensuring a force convergence
503 threshold of 20 meV $Å^{-1}$. The calculated bulk lattice parameters of Li are a=b=c=3.4727 Å, which
504 are in good agreement with the experimental Li lattice parameters (a=b=c=3.48 Å).[57] For Li_2O,
505 the optimized lattice parameters, a=b=c= 4.567 Å, closely aligned with the theoretically
506 extrapolated lattice parameters of a=b=c=4.573 Å at T = 0 K, which is approximately 0.05 Å
507 smaller than the experimentally measured room-temperature value, 4.619 Å.[58,59] For Li_2CO_3, the
508 optimized lattice parameters (a = 8.318 Å, b = 4.982 Å, and c = 6.055 Å) closely match the
509 experimental values (a = 8.355 Å, b = 4.991 Å, and c = 6.139 Å), demonstrating good agreement
510 between the computational and experimental results.[60] Surface models were optimized using a
511 plane-wave cutoff energy of 400 eV and a 2 × 2 × 1 k-point mesh within the Monkhorst-Pack
512 scheme, with the bottom three atomic layers constrained. The self-consistent field (SCF) iterations
513 were terminated upon reaching a convergence criterion of 1×10^{-5} eV, while ionic relaxation was
514 completed when the forces on all atoms were below –0.03 eV/Å. Gas-phase molecular energies

and geometries were determined by placing the molecules in a cubic simulation box of 30 × 30 × 30 $Å^3$, employing a single Γ-point for the calculations.

ASSOCIATED CONTENT

Supporting Information. The following files are available free of charge.

AUTHOR INFORMATION

Corresponding Author

*Correspondence: dhkang@anl.gov

**Correspondence: jelam@anl.gov

Author Contributions

All of the authors have given approval to the final version of the manuscript.

Notes

The authors declare no competing financial interest.

ACKNOWLEDGMENT

This material is based upon work supported by Laboratory Directed Research and Development (LDRD) funding from Argonne National Laboratory, provided by the Director, Office of Science, of the U.S. Department of Energy under Contract No. DE-AC02-06CH11357. Work performed at the Center for Nanoscale Materials, a U.S. Department of Energy Office of Science User Facility, was supported by the U.S. DOE, Office of Basic Energy Sciences, under Contract No. DE-AC02-06CH11357. The computational study is supported by the U.S. DOE, Office of Basic Energy

Sciences, Division of Chemical Sciences, Geosciences, and Biosciences, under contract No. DE-AC02-06CH11357. All the calculations were conducted using computational resources from the Laboratory Computing Research Center (LCRC) at Argonne National Laboratory and the National Energy Research Scientific Computing Center (NERSC), supported under Contract No. DE-AC02-05CH11231 with NERSC award BES-ERCAP0033589. UV Raman spectroscopy was supported by the US DOE, Office of Science, Office of Basic Energy Sciences, ICEP program at Northwestern University, under Grant Number DE-FG02-03ER15457.

REFERENCES

1. Liu, D., Wu, B., Xu, Y., Ellis, J., Baranovskiy, A., Lu, D., Lochala, J., Anderson, C., Baar, K., Qu, D., et al. Controlled large-area lithium deposition to reduce swelling of high-energy lithium metal pouch cells in liquid electrolytes. Nat. Energy **2024**, *9*, 559-569. DOI: 10.1038/s41560-024-01488-9.

2. Deysher, G., Oh, J.A.S., Chen, Y.-T., Sayahpour, B., Ham, S.-Y., Cheng, D., Ridley, P., Cronk, A., Lin, S.W.-H., Qian, K., et al. Design principles for enabling an anode-free sodium all-solid-state battery. Nat. Energy **2024** *9*, 1161-1172. DOI: 10.1038/s41560-024-01569-9.

3. Oyakhire, S.T., and Bent, S.F. Interfacial engineering of lithium metal anodes: what is left to uncover? Energy Adv. **2024**, *3*, 108-122. DOI: 10.1039/d3ya00470h.

4. Yoon, K., Lee, S., Oh, K., and Kang, K. Challenges and Strategies towards Practically Feasible Solid-State Lithium Metal Batteries. Adv. Mater. **2022**, *34*, 2104666. DOI: 10.1002/adma.202104666.

5. Yuan, H., Ding, X., Liu, T., Nai, J., Wang, Y., Liu, Y., Liu, C., and Tao, X. A review of concepts and contributions in lithium metal anode development. Mater. Today **2022**, *53*, 173-196. DOI: 10.1016/j.mattod.2022.01.015.

6. Fang, C., Wang, X., and Meng, Y.S. Key Issues Hindering a Practical Lithium-Metal Anode. Trends Chem. **2019**, *1*, 152-158. DOI: 10.1016/j.trechm.2019.02.015.

7. Liu, J., Bao, Z., Cui, Y., Dufek, E.J., Goodenough, J.B., Khalifah, P., Li, Q., Liaw, B.Y., Liu, P., Manthiram, A., et al. Pathways for practical high-energy long-cycling lithium metal batteries. Nat. Energy **2019**, *4*, 180-186. DOI: 10.1038/s41560-019-0338-x.

8. T. H. Westmore, H. B. Eitouni, A. Nuval, R. C. Pratt. **2019**, US20190280292A1.

9. Wu, W., Luo, W., and Huang, Y. Less is more: a perspective on thinning lithium metal towards high-energy-density rechargeable lithium batteries. Chem. Soc. Rev. **2023**, *52*, 2553-2572. DOI: 10.1039/D2CS00606E.

10. Acebedo, B., Morant-Miñana, M.C., Gonzalo, E., Ruiz de Larramendi, I., Villaverde, A., Rikarte, J., and Fallarino, L. Current Status and Future Perspective on Lithium Metal Anode Production Methods. Adv. Energy Mater. **2023**, *13*, 2203744. DOI: 10.1002/aenm.202203744.

11. Zhao, Y., Amirmaleki, M., Sun, Q., Zhao, C., Codirenzi, A., Goncharova, L.V., Wang, C., Adair, K., Li, X., Yang, X., et al. Natural SEI-Inspired Dual-Protective Layers via Atomic/Molecular Layer Deposition for Long-Life Metallic Lithium Anode. Matter **2019**, *1*, 1215-1231. DOI: 10.1016/j.matt.2019.06.020.

12. Wang, H., Yi, Z.-L., Su, F.-Y., Song, G., Xie, L.-J., Wang, Z.-B., and Chen, C.-M. The effect of removing the native passivation film on the electrochemical performance of lithium metal electrodes. J. Power Sources **2022**, *520*, 230817. DOI: 10.1016/j.jpowsour.2021.230817.

13. Kazyak, E., Wood, K.N., and Dasgupta, N.P. Improved Cycle Life and Stability of Lithium Metal Anodes through Ultrathin Atomic Layer Deposition Surface Treatments. Chem. Mater. **2015**, *27*, 6457-6462. DOI: 10.1021/acs.chemmater.5b02789.

14. Chen, L., Connell, J.G., Nie, A., Huang, Z., Zavadil, K.R., Klavetter, K.C., Yuan, Y., Sharifi-Asl, S., Shahbazian-Yassar, R., Libera, J.A., et al. Lithium metal protected by atomic layer deposition metal oxide for high performance anodes. J. Mater. Chem. A **2017**, *5*, 12297-12309. DOI: 10.1039/C7TA03116E.

15. Kozen, A.C., Lin, C.-F., Pearse, A.J., Schroeder, M.A., Han, X., Hu, L., Lee, S.-B., Rubloff, G.W., and Noked, M. Next-Generation Lithium Metal Anode Engineering via Atomic Layer Deposition. ACS Nano **2015**, *9*, 5884-5892. DOI: 10.1021/acsnano.5b02166.

16. Alaboina, P.K., Rodrigues, S., Rottmayer, M., and Cho, S.-J. In Situ Dendrite Suppression Study of Nanolayer Encapsulated Li Metal Enabled by Zirconia Atomic Layer Deposition. ACS Appl. Mater. Interfaces **2018**, *10*, 32801-32808. DOI: 10.1021/acsami.8b08585.

17. Chen, L., Chen, K.-S., Chen, X., Ramirez, G., Huang, Z., Geise, N.R., Steinrück, H.-G., Fisher, B.L., Shahbazian-Yassar, R., Toney, M.F., et al. Novel ALD Chemistry Enabled Low-Temperature Synthesis of Lithium Fluoride Coatings for Durable Lithium Anodes. ACS Appl. Mater. Interfaces **2018**, *10*, 26972-26981. DOI: 10.1021/acsami.8b04573.

18. Xie, J., Liao, L., Gong, Y., Li, Y., Shi, F., Pei, A., Sun, J., Zhang, R., Kong, B., Subbaraman, R., et al. Stitching h-BN by atomic layer deposition of LiF as a stable interface for lithium metal anode. Sci. Adv. **2017**, *3*, eaao3170. DOI: 10.1126/sciadv.aao3170.

19. Niu, J., Wang, M., Cao, T., Cheng, X., Wu, R., Liu, H., Zhang, Y., and Liu, X. Li metal coated with Li_3PO_4 film via atomic layer deposition as battery anode. Ionics **2021**, *27*, 2445-2454. DOI: 10.1007/s11581-021-04030-z.

20. Cao, Y., Meng, X., and Elam, J.W. Atomic Layer Deposition of LiAlS Solid-State Electrolytes for Stabilizing Lithium-Metal Anodes. ChemElectroChem **2016**, *3*, 858-863. DOI: 10.1002/celc.201600139.

21. Kang, D., Warburton, R.E., Mane, A.U., Greeley, J., and Elam, J.W. Modification of $LiMn_2O_4$ surfaces by controlling the Acid–Base surface chemistry of atomic layer deposition. Appl. Surf. Sci. **2022**, *599*, 153329. DOI: 10.1016/j.apsusc.2022.153329.

22. Otto, S.-K., Moryson, Y., Krauskopf, T., Peppler, K., Sann, J., Janek, J., and Henss, A. In-Depth Characterization of Lithium-Metal Surfaces with XPS and ToF-SIMS: Toward Better Understanding of the Passivation Layer. Chem. Mater. **2021**, *33*, 859-867. DOI: 10.1021/acs.chemmater.0c03518.

23. Sauerbrey, G. Verwendung von Schwingquarzen zur Wägung dünner Schichten und zur Mikrowägung. Zeitschrift für Physik **1959**, *155*, 206-222. DOI: 10.1007/BF01337937.

24. Kim, J., Urchaga, P., Baranton, S., Coutanceau, C., and Jerkiewicz, G. Interfacial structure of atomically flat polycrystalline Pt electrodes and modified Sauerbrey equation. PCCP **2017**, *19*, 21955-21963. DOI: 10.1039/C7CP02528A.

25. Elam, J.W., and George, S.M. Growth of ZnO/Al_2O_3 Alloy Films Using Atomic Layer Deposition Techniques. Chem. Mater. **2003**, *15*, 1020-1028. DOI: 10.1021/cm020607+.

26. Greczynski, G., and Hultman, L. The same chemical state of carbon gives rise to two peaks in X-ray photoelectron spectroscopy. Sci. Rep. **2021**, *11*, 11195. DOI: 10.1038/s41598-021-90780-9.

27. Tan, Y.-H., Lu, G.-X., Zheng, J.-H., Zhou, F., Chen, M., Ma, T., Lu, L.-L., Song, Y.-H., Guan, Y., Wang, J., et al. Lithium Fluoride in Electrolyte for Stable and Safe Lithium-Metal Batteries. Adv. Mater. **2021**, *33*, 2102134. DOI: 10.1002/adma.202102134.

28. Qiao, L., Oteo, U., Martinez-Ibañez, M., Santiago, A., Cid, R., Sanchez-Diez, E., Lobato, E., Meabe, L., Armand, M., and Zhang, H. Stable non-corrosive sulfonimide salt for 4-V-class lithium metal batteries. Nat. Mater. **2022**, *21*, 455-462. DOI: 10.1038/s41563-021-01190-1.

29. Robertson, J. Diamond-like amorphous carbon. Materials Science and Engineering: R: Reports **2022**, *37*, 129-281. DOI: 10.1016/S0927-796X(02)00005-0.

30. Saito, R., Hofmann, M., Dresselhaus, G., Jorio, A., and Dresselhaus, M.S. Raman spectroscopy of graphene and carbon nanotubes. Adv. Phys. **2011**, *60*, 413-550. DOI: 10.1080/00018732.2011.582251.

31. Zhang, Z., Pan, Y., Yang, J., Jiang, Z., and Fang, H. Experimental study of trimethyl aluminum decomposition. J. Cryst. Growth **2017**, *473*, 6-10. DOI: 10.1016/j.jcrysgro.2017.05.020.

32. Itatani, K., Hasegawa, M., Aizawa, M., Howell, F.S., Kishioka, A., and Kinoshita, M. Some Properties of Aluminum Carbide Powder Prepared by the Pyrolysis of Alkylaluminu. J. Am. Ceram. Soc. **1995**, *78*, 801-804. DOI: 10.1111/j.1151-2916.1995.tb08250.x.

33. Squire, D.W., Dulcey, C.S., and Lin, M.C. Mechanistic studies of the decomposition of trimethylaluminum on heated surfaces. J. Vac. Sci. Technol. B. **1985**, *3*, 1513-1519. DOI: 10.1116/1.582976.

34. Goldstein, D. N.; McCormick, J. A.; George, S. M. Al2O3 Atomic Layer Deposition with Trimethylaluminum and Ozone Studied by in Situ Transmission FTIR Spectroscopy and Quadrupole Mass Spectrometry. *J. Phys. Chem. C* **2008**, *112* (49), 19530-19539. DOI: 10.1021/jp804296a.

35. Zhao, Q., Deng, Y., Utomo, N.W., Zheng, J., Biswal, P., Yin, J., and Archer, L.A. On the crystallography and reversibility of lithium electrodeposits at ultrahigh capacity. Nat. Commun. **2021**, *12*, 6034. DOI: 10.1038/s41467-021-26143-9.

36. Liu, Z., Qi, Y., Lin, Y.X., Chen, L., Lu, P., and Chen, L.Q. Interfacial Study on Solid Electrolyte Interphase at Li Metal Anode: Implication for Li Dendrite Growth. J. Electrochem. Soc. **2016**, *163*, A592. DOI: 10.1149/2.0151605jes.

37. Yuan, Z., Kong, X., Ma, S., Gao, T., Xiao, C., Chen, X., and Lu, T. Adsorption and diffusion mechanism of hydrogen atom on the Li_2O (111) and (110) surfaces from first principles calculations. J. Nucl. Mater. **2019**, *513*, 232-240. DOI: 10.1016/j.jnucmat.2018.11.008.

38. Islam, M.M., and Bredow, T. Density Functional Theory Study for the Stability and Ionic Conductivity of Li2O Surfaces. J. Phys. Chem. C **2009**, *113*, 672-676. DOI: 10.1021/jp807048p.

39. Zhu, J., Fang, Y., Xiao, H., Chen, X., Gao, T., and Xiao, C. First-Principles Study of the Effect of Doped Metal Atoms Pd, Mg and Ti on Tritium Release from Li_2O (111) Surface. Comput. Mater. Sci. **2019**, *188*, 110151. DOI: 10.1016/j.commatsci.2020.110151.

40. Kong, X., Yu, Y., Ma, S., Gao, T., Xiao, C., and Chen, X. Dissociation mechanism of H_2 molecule on the Li_2O/hydrogenated-Li_2O (111) surface from first principles calculations. RSC Adv. **2017**, *7*, 35239-35250. DOI: 10.1039/C7RA05894B.

41. Bruno, M., and Prencipe, M. Ab initio quantum-mechanical modeling of the (001), ($1\bar{}01$) and (110) surfaces of zabuyelite (Li_2CO_3). Surf. Sci. **2007**, *601*, 3012-3019. DOI: 10.1016/j.susc.2007.05.004.

42. Kulathuvayal, A.S., and Su, Y. Ionic Transport through the Solid Electrolyte Interphase in Lithium-Ion Batteries: A Review from First-Principles Perspectives. ACS Appl. Energy Mater. **2023**, *6*, 5628-5645. DOI: 10.1021/acsaem.3c00287.

43. Ahmad, Z., Venturi, V., Hafiz, H., and Viswanathan, V. Interfaces in Solid Electrolyte Interphase: Implications for Lithium-Ion Batteries. J. Phys. Chem. C **2021**, *125*, 11301-11309. DOI: 10.1021/acs.jpcc.1c00867.

44. Larrabee, T.J., Mallouk, T.E., and Allara, D.L. An atomic layer deposition reactor with dose quantification for precursor adsorption and reactivity studies. Rev. Sci. Instrum. **2013**, *84*, 014102. DOI: 10.1063/1.4774042.

45. Lee, Y.-G., Fujiki, S., Jung, C., Suzuki, N., Yashiro, N., Omoda, R., Ko, D.-S., Shiratsuchi, T., Sugimoto, T., Ryu, S., et al. High-energy long-cycling all-solid-state lithium metal batteries enabled by silver–carbon composite anodes. Nat. Energy **2020**, *5*, 299-308. DOI: 10.1038/s41560-020-0575-z.

46. Zhang, R., Chen, X., Shen, X., Zhang, X.-Q., Chen, X.-R., Cheng, X.-B., Yan, C., Zhao, C.-Z., and Zhang, Q. Coralloid Carbon Fiber-Based Composite Lithium Anode for Robust Lithium Metal Batteries. Joule **2018**, *2*, 764-777. DOI: 10.1016/j.joule.2018.02.001.

47. Ely, D.R., and García, R.E. Heterogeneous Nucleation and Growth of Lithium Electrodeposits on Negative Electrodes. J. Electrochem. Soc. **2013**, *160*, A662. DOI: 10.1149/1.057304jes.

48. Liu, Y., Xu, X., Sadd, M., Kapitanova, O.O., Krivchenko, V.A., Ban, J., Wang, J., Jiao, X., Song, Z., Song, J., et al. Insight into the Critical Role of Exchange Current Density on Electrodeposition Behavior of Lithium Metal. Adv. Sci. **2021**, *8*, 2003301. DOI: 10.1002/advs.202003301.

49. Han, S., Li, Z., Zhang, Y., Lei, D., and Wang, C. In-situ formation of a nanoscale lithium aluminum alloy in lithium metal for high-load battery anode. Energy Storage Mater. **2022**, *48*, 384-392. DOI: 10.1016/j.ensm.2022.03.036.

50. Chen, S., Yang, X., Zhang, J., Ma, J., Meng, Y., Tao, K., Li, F., and Geng, J. Aluminum−lithium alloy as a stable and reversible anode for lithium batteries. Electrochim. Acta **2021**, *368*, 137626. DOI: 10.1016/j.electacta.2020.137626.

51. Futscher, M.H., Amelal, T., Sastre, J., Müller, A., Patidar, J., Aribia, A., Thorwarth, K., Siol, S., and Romanyuk, Y.E. Influence of amorphous carbon interlayers on nucleation and early growth of lithium metal at the current collector-solid electrolyte interface. J. Mater. Chem. A **2022**, *10*, 15535-15542. DOI: 10.1039/D2TA02843C.

52. Feng, W., Dong, X., Zhang, X., Lai, Z., Li, P., Wang, C., Wang, Y., and Xia, Y. Li/Garnet Interface Stabilization by Thermal-Decomposition Vapor Deposition of an Amorphous Carbon Layer. Angew. Chem. Int. Ed. **2020**, *59*, 5346-5349. DOI: 10.1002/anie.201915900.

53. Chen, L., Zhang, J., Tong, R.-A., Zhang, J., Wang, H., Shao, G., and Wang, C.-A. Excellent Li/Garnet Interface Wettability Achieved by Porous Hard Carbon Layer for Solid State Li Metal Battery. Small **2022**, *18*, 2106142. DOI: 10.1002/smll.202106142.

54. Elam, J.W., Groner, M.D., and George, S.M. Viscous flow reactor with quartz crystal microbalance for thin film growth by atomic layer deposition. Rev. Sci. Instrum. **2002**, *73*, 2981-2987. DOI: 10.1063/1.1490410.

55. Young, M.J., Letourneau, S., Warburton, R.E., Dose, W.M., Johnson, C., Greeley, J., and Elam, J.W. High-Rate Spinel $LiMn_2O_4$ (LMO) Following Carbonate Removal and Formation of Li-Rich Interface by ALD Treatment. J. Phys. Chem. C **2019**, *123*, 23783-23790. DOI: 10.1021/acs.jpcc.9b04418.

56. Kim, H., Kosuda, K.M., Van Duyne, R.P., and Stair, P.C. Resonance Raman and surface- and tip-enhanced Raman spectroscopy methods to study solid catalysts and heterogeneous catalytic reactions. Chem. Soc. Rev. **2010**, *39*, 4820-4844. DOI: 10.1039/C0CS00044B.

57. Anderson, M.S., and Swenson, C.A. Experimental equations of state for cesium and lithium metals to 20 kbar and the high-pressure behavior of the alkali metals. Phys. Rev. B. **1985**, *31*, 668-680. DOI: 10.1103/PhysRevB.31.668.

58. Islam, M.M., Bredow, T., and Minot, C. Theoretical Analysis of Structural, Energetic, Electronic, and Defect Properties of Li_2O. The Journal of Physical Chemistry B **2006**, *110*, 9413-9420. DOI: 10.1021/jp0566764.

59. Hull, S., Farley, T.W.D., Hayes, W., and Hutchings, M.T. The elastic properties of lithium oxide and their variation with temperature. J. Nucl. Mater. *160*, **1988**, 125-134. DOI: 10.1016/0022-3115(88)90039-6.

60. Idemoto, Y., Richardson, J.W., Koura, N., Kohara, S., and Loong, C.-K. Crystal structure of $(Li_xK_{1-x})_2CO_3$ (x = 0, 0.43, 0.5, 0.62, 1) by neutron powder diffraction analysis. J. Phys. Chem. Solids **1998**, *59*, 363-376. DOI: 10.1016/S0022-3697(97)00209-6.

725 TABLE OF CONTENTS

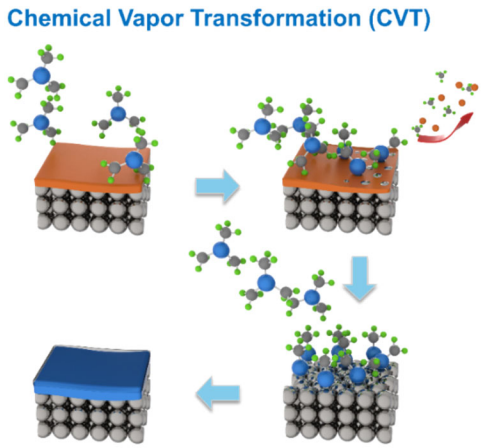

726

727